Tribology International 131 (2019) 424–437

Contents lists available at ScienceDirect

Tribology International

journal homepage: www.elsevier.com/locate/triboint

Boundary friction characterisation of a used cylinder liner subject to fired engine conditions and surface deposition

S.R. Bewsher[a,*], M. Leighton[a], M. Mohammadpour[a], H. Rahnejat[a], G. Offner[b], O. Knaus[b]

[a] Wolfson School of Mechanical, Electrical and Manufacturing Engineering, Loughborough University, Loughborough, LE113TU, England, UK
[b] AVL List GmbH, Graz, Austria

ARTICLE INFO

Keywords:
Boundary friction
Atomic Force Microscope (AFM)
X-ray photoelectron spectroscopy (XPS)
Lubricant-surface combination

ABSTRACT

For future engines to become more efficient, with enhanced fuel economy and increased power output, accurate prediction of new designs is required over the full lifetime of an engine. The analysis uses of a local pressure coefficient of boundary shear strength of asperities value, taking into account the localised effects of surface texture, coating and surface deposition. XPS spectra analysis was also carried out to identify the surface depositions as a result of combustion, not previously taken into account during piston ring pack simulation. It was found that piston varnish on the liner corresponded to higher values of the pressure coefficient of boundary shear strength of asperities, showing the importance of using real system components run under representative operating conditions.

1. Introduction

Reduction of friction and wear are key tribological objectives when designing new components and seeking new lubricant-surface combinations for Internal Combustion (IC) engines. Improvements in tribological performance can lead to better fuel economy, increased power output and reduced consumption of oil. Accurate simulation plays a key role during the research and development phase of the IC engine design processes. This is of particular importance given that up to one third of the fuel energy is used to overcome friction in the engine, transmission, tyres and brakes in medium size passenger vehicles, trucks and buses [1,2]. For medium sized passenger vehicles, excluding the brake friction it is estimated that the direct frictional losses contribute as much as 28% of the total fuel energy [1]. The largest contributor to these frictional losses is the piston assembly, found to contribute on average 45% of these losses [1,2].

Emissions and engine efficiency are known to be affected by deposits which form as a result of combustion by-products. Three key components making up particulates in diesel engines are: solids (principally carbon in its elemental forms), a soluble organic fraction (normally partially burnt fuel and oil from lubrication), and sulphates [3]. Shurvell et al. [4] found that the deposits are typically a mixture of inorganic material (ash), carbonaceous products (soot) and an organic resin. The relationship between the wear of cylinder liners and the sulphur content in diesel fuels has been widely documented in literature. The sulphuric acid which arises as a result of SO_x combustion by-products can lead to corrosive wear and abrasion of the liner. The lubricants used in diesel engines use refined base oil with a mix of additives, some of which are applied to protect the lubricant system from combustion by-products, such as detergents [5].

The build-up of carbonaceous deposits over time can prevent the piston rings performing as effective seals against combustion gases. Thus alkaline detergents are used as neutralisers, helping to clean and remove any deposits left behind on hot metal surfaces. One type of carbonaceous deposit is known as piston varnish, appearing as light amber in colour. It is typically found on piston skirts and made up of oxidised hydrocarbons [6]. Varnish occurs as a result of products from lubricant polymerisation becoming insoluble in the lubricant and reacting with the metallic surfaces of engine components on which they deposit. The polymerisation and varnish processes are complex and multivariable and increase with temperature.

The accumulation of soot as a result of combustion also increases the wear of cylinder liners. Soot can also absorb oil additives, preventing the formation of anti-wear films on the contacting surfaces, thus increasing the rate of wear of liner [5]. Bore polishing occurs as a result of carbon deposition at the top ring reversal point. Carbon particles can also get stuck between the ring and ring groove interfaces, resulting in reduced clearance. This can result in unwanted wear, scuffing and sticking as well as increased blow-by.

IC engines have many varying operating conditions during their

* Corresponding author.
E-mail address: s.r.bewsher@lboro.ac.uk (S.R. Bewsher).

https://doi.org/10.1016/j.triboint.2018.11.005
Received 2 July 2018; Received in revised form 18 September 2018; Accepted 7 November 2018
Available online 13 November 2018

Nomenclature

A	Apparent contact area (m^2)
A_a	Asperity contact area (m^2)
E'	Composite (reduced) Young's modulus of elasticity of contact (GPa)
b	Ring face-width (axial direction) (mm)
c	Ring crown height (μm)
d	Ring thickness (radial direction) (mm)
f	Total friction (N)
f_b	Boundary friction (N)
f_v	Viscous friction (N)
F	Contact load (N)
F_2	Statistical function
$F_{5/2}$	Statistical function
F_e	Ring elastic force (N)
F_g	Gas force (N)
g	Ring end gap (mm)
h	Lubricant film thickness (μm)
h_m	Minimum film thickness (μm)
h_s	The ring axial profile (mm)
I	Second area moment of inertia (m^4)
k	Ratio of surface velocities
l	Ring circumference (mm)
ℓ	Connecting rod length (mm)
n	Number of iteration
p	Gauge pressure (Pa)
p_e	Elastic pressure (Pa)
P_a	Pressure at the conjunction inlet (Pa)
P_c	Combustion pressure (Pa)
P_{cav}	Cavitation pressure (Pa)
r	Crankpin radius (mm)
r_0	Nominal bore radius (mm)
S_0	Temperature-viscosity index
t	Time (s)
U	Sliding velocity (axial direction) (ms^{-1})
V	Lateral velocity (radial direction) (ms^{-1})
W	Total contact reaction force (N)
W_a	Load carried by the asperities (N)
W_h	Hydrodynamic reaction force (N)
x	Direction along the ring face width
x_c	Lubricant film rupture point (mm)
y	Direction along the bore circumference
Z	Pressure-viscosity index

Greek Symbols

α	Pressure-viscosity coefficient (m^2N^{-1})
α^*	Modified pressure-viscosity coefficient (m^2N^{-1})
ζ	Number of asperities per unit area of contact (asperity density) (m^{-2})
φ	Crank angle (rad)
η	Dynamic viscosity of the lubricant ($kgm^{-1}s^{-1}$)
η_0	Dynamic viscosity of the lubricant in atmospheric conditions ($kgm^{-1}s^{-1}$)
θ	Liner temperature (K)
θ_0	Reference temperature (K)
κ	Average asperity tip radius of curvature (m)
K	Conformability coefficient (factor)
λ	Stribeck's parameter
ρ	Lubricant density (kgm^{-3})
ρ_0	Lubricant density at atmospheric pressure (kgm^{-3})
σ	Composite surface roughness (m)
ς	Boundary shear strength of asperities
τ	Shear stress (Pa)
τ_0	Eyring shear stress (MPa)
Ψ	AFM-specific overall calibration factor
ω	Engine speed ($rads^{-1}$)

lifetime which can affect the power losses as the result of friction. Lubricant manufacturers often reduce the lubricant viscosity in order to mitigate overall friction within contacting components, through decreased viscous shear [7]. However, it has been shown that during the combustion stroke boundary interactions dominate, thus boundary friction should also be considered [8]. In order to take into account the asperity contact within a conjunction the Greenwood and Tripp method can be used [9,10], for which evaluation of boundary shear strength of asperities, ς is required. The value of ς can be measured using an Atomic Force Microscope (AFM) in Lateral Force Mode (LFM). In reality, ς is dependent on a fully formulated lubricant in combination with the surfaces in contact under operating conditions. It is also dependent on the component history as having been exposed to varying operating conditions and tribo-films of lubricant additives are adsorbed/bonded to the contacting surfaces.

Many analyses are available in literature where a single value of ς is used in order to calculate the boundary friction contribution. This value is typically found by taking a polished, flat idealised sample in conjunction with a base oil in a controlled environment, which is not representative of an actual engine component under operating conditions. The work carried out in this study uses a cylinder liner from a modern IC engine which has run for 105,000 miles under urban driving cycle with a fully formulated existing lubricant with a complete additive package. The measured data is used to show the variation of ς along the stroke providing more reliable input data for the simulations presented. This paper presents a unique analysis of how the deposition of combustion by-product and any resulting tribo-film in different positions along the cylinder liner affect the boundary interaction and thus frictional characteristics of the conjunction. It also shows that the obtained values vary in different positions along the liner due to different working conditions and depositions.

2. Specification of the lubricant and cylinder liner

The cylinder liner used as the test specimen in this study is taken from an engine which has undergone a full durability engine test. Fig. 1 shows the section which has been cut for the purpose of analysis, with the material properties provided in Table 1. This study is limited to

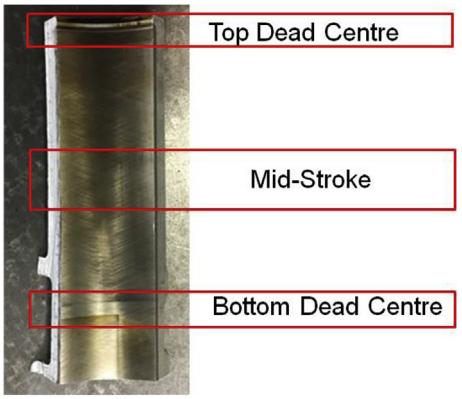

Fig. 1. Section of the cylinder liner which has been cut out for analysis and experimentation with defined zones for analysis.

Table 1
Material properties of the cylinder liner.

Parameters	Values	Units
Liner material	Grey cast iron	–
Modulus of elasticity of the liner	120	GPa
Poisson's ratio of the liner	0.28	–
Hardness (H)	2325	MPa
Density of the liner material	7200	kg/m^3
Engine testing condition	105000	Miles

Table 2
Lubricant properties.

Parameters	Values	Units
SAE grade	5W-20	–
Viscosity @100 °C	8.9	cSt
Viscosity @40 °C	49.8	cSt
Viscosity index	160	
Sulphated ash	0.85	wt%
High temperature high shear viscosity @150 °C	2.75	mPa.s
Pour point	−43	°C
Flash point	230	°C
Density @15 °C	0.852	g/ml

Table 3
Lateral force microscopy settings on the AFM.

Parameter	Value
Scan area	4 × 1 μm^2
Scan rate	2 Hz
Samples	1024 × 256
Scan angle (Friction)	90°

Table 4
AFM probe specification.

Model	DNP-10
Material	Non-Conductive Silicon Nitride
K	0.350 Nm^{-1}
Nominal tip radius	20 nm

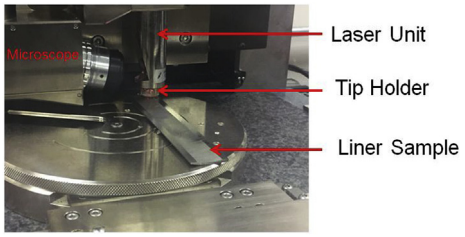

Fig. 2. Cylinder liner specimen under dry contact AFM.

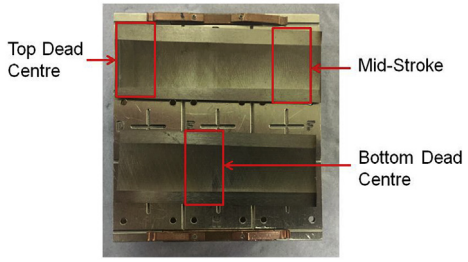

Fig. 3. Cylinder liner prepared for XPS analysis.

three defined regions of the cylinder liner:

- Top Dead Centre (TDC), the region where starvation occurs due to piston reversal between the top compression and the scraper rings. At TDC the compression ring is subject to higher contact pressures and boundary friction as a result of combustion.
- Mid-Stroke where the largest amount of viscous shear occurs due to increased sliding speed.
- The Bottom Dead Centre (BDC), subjected to the minimum contact pressure which can also be subjected to starvation. The three regions are shown in Fig. 1.

For the purpose of this study, and in order to carry out the wet AFM required to find the boundary shear strength of asperities, ς, Mobil 1 Super 3000 5W-20 has been used under ambient conditions, as it is not possible to replicate the engine temperatures on the AFM. This is a fully formulated lubricant with an additive package and is the same as that used during the engine testing which was conducted previously. The lubricant properties can be found in Table 2 below.

3. Experimental procedure

3.1. Atomic force microscopy

A Veeco Dimension 3100 AFM is used in lateral mode (LFM) to measure ς [11–14] in the defined zones of the cylinder liner surface. The settings of AFM are listed in Table 3 with the probe specification shown in Table 4. The experimental set up can be seen in Fig. 2. AFM is deemed to be an appropriate methodology as the roughness scale is independent due to such a small scan area which is significantly smaller than that of optical measurement techniques (for example Alicona has a pixel size of 1,74 × 1.74 μm with ×100 optic lens).

A silicon wafer with known surface characteristics is used for calibration of the AFM ($\varsigma_{Si} = 0.19 \pm 0.1$) [15]. Since the stiffness of the tip is known, it is possible to follow the methodology outlined by Buenviaje et al. [16] to perform a blind calibration and find a value of ψ. The same calibration methodology is followed for both wet and dry LFM analyses.

3.2. X-ray photoelectron spectroscopy

In order to analyse the surface deposition in each of the three regions of the cylinder liner, a Thermo Scientific K-Alpha ESCA XPS is used. XPS can typically be used to find the compositional and chemical state of a material between 3 and 10 nm deep into the surface using an ion beam [17]. It should be noted that XPS is unable to pick up Hydrogen elements. For the purpose of this study, this is acceptable as the deposits formed on the liner surface termed as varnish tend to be carbon-based. XPS can also be used to find any changes such as oxidation or composition of elements. Within the materials industry, XPS is commonly used to study thin films, corrosive and adhesive products and thus it is believed suitable for cylinder liner surface to study deposits.

For the tests carried out the operating range of the Ion Gun was set in the range 4–100 eV with a maximum analysis area of 60 × 60 mm^2. Nine scans were carried out initially for each region to gain an understanding of what could be observed on the surface, followed by high resolution XPS, where investigations were directed for specific deposited/bonded elements based upon the original findings. It was necessary to cut the liner once more for it to fit into the XPS. This is shown in Fig. 3.

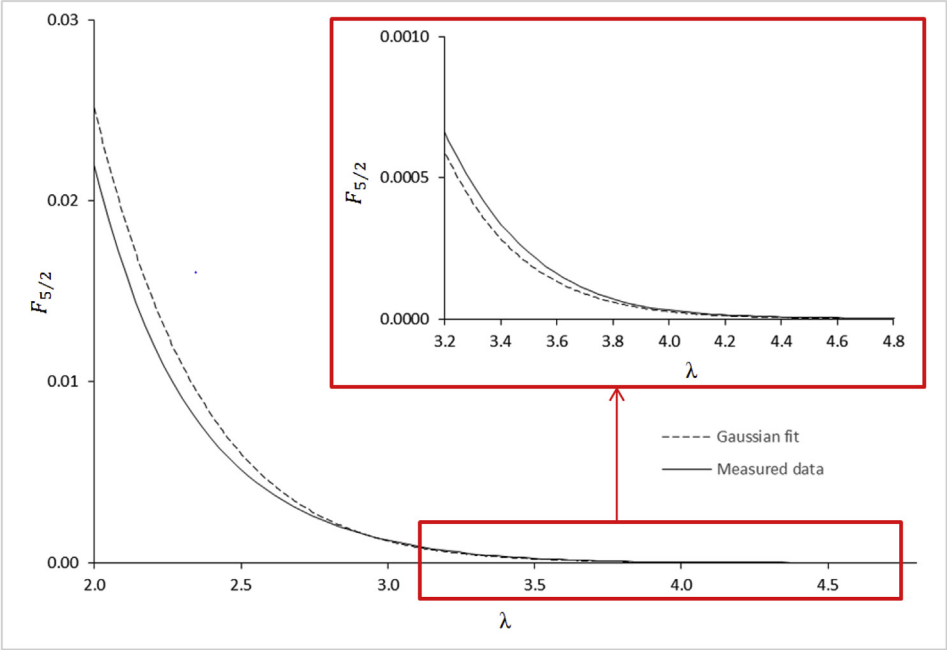

Fig. 4. $F_{5/2}(\lambda)$ function plotted to show the agreement between the measured and theoretical Gaussian peak height distribution.

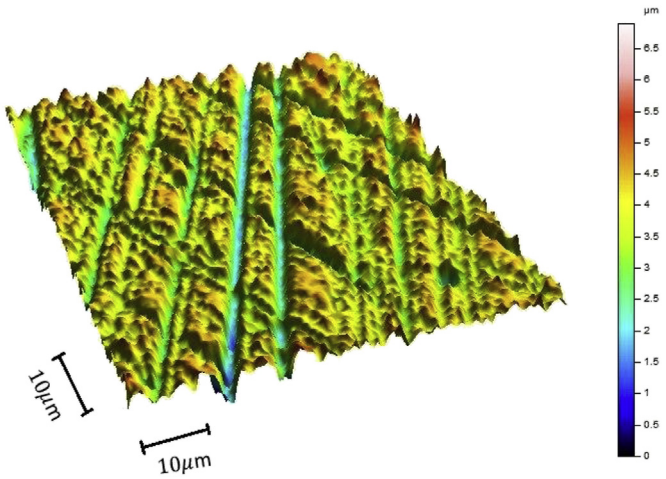

Fig. 5. An example of surface roughness data obtained using the Alicona G4 microscope.

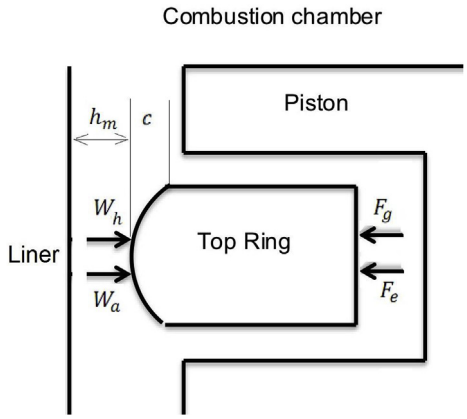

Fig. 6. Radially applied forces acting on a compression ring.

4. Mixed-lubrication model for the piston ring – cylinder liner conjunction

4.1. Asperity contact pressure

In order to predict conjunctional friction, a numerical model is devised to calculate boundary friction and viscous friction contributions, thus:

$$f = f_v + f_b \tag{1}$$

In order to calculate the boundary friction f_b, it is also necessary to find the asperity load, W_a, and the area occupied by asperities A_a [18],:

$$f_b = \tau_0 A_a + \varsigma W_a \tag{2}$$

τ_0, the Eyring Stress of the oil, can be measured by carrying out high shear viscometry and is an underlying lubricant property. For the purposes of this study τ_0 was taken to be 2 MPa [19] The procedure used to find ς, the shear strength of asperities, is experimentally using an AFM. It is dependent on the specific lubricant-surface combination [20,21].

W_a and A_a are load carried by asperities and their contact area within the apparent contact. They can be obtained as [9]:

$$W_a = \frac{16\sqrt{2}}{15}\pi(\zeta\kappa\sigma)^2\sqrt{\frac{\sigma}{\kappa}}E'AF_{5/2}(\lambda) \tag{3}$$

$$A_a = \pi^2(\zeta\kappa\sigma)^2\sqrt{\frac{\sigma}{\kappa}}AF_2(\lambda) \tag{4}$$

These formulae are taken from the Greenwood and Tripp contact model [9,10], whereby the roughness parameter $\zeta\kappa\sigma$, can be found using surface topographical measurements. The typical asperity slope is shown as $\frac{\sigma}{\kappa}$ [9,10]. The statistical functions used in this analysis, $F_2(\lambda)$ and $F_{5/2}(\lambda)$, have been found by fitting a Gaussian distribution to the peak height distribution averaged from 5 surface areas measured. This resulted in a good fit with probabilistic function in the region $2 < \lambda < 4.8$. This corresponds to the region from the highest peak on the surfaces measured ($\lambda \approx 4.8$) to a film thickness ratio which would correspond to severe mixed or boundary regime. This range covers the regimes that the piston rings and skirt operate in IC engines. A sixth order polynomial, fitted to the data, was then implemented into the

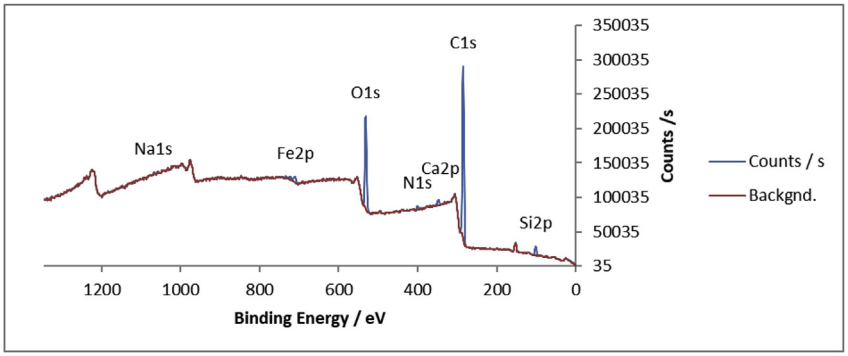

Fig. 7. XPS spectra analysis of TDC.

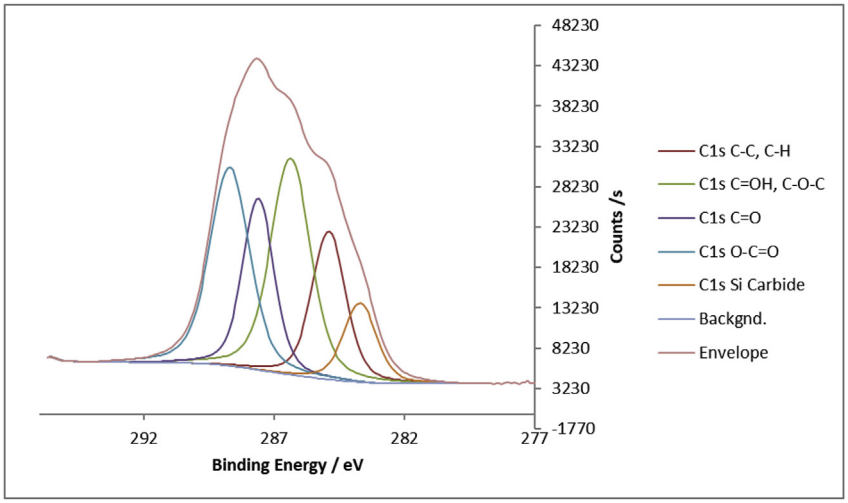

Fig. 8. High resolution C1s scan at TDC.

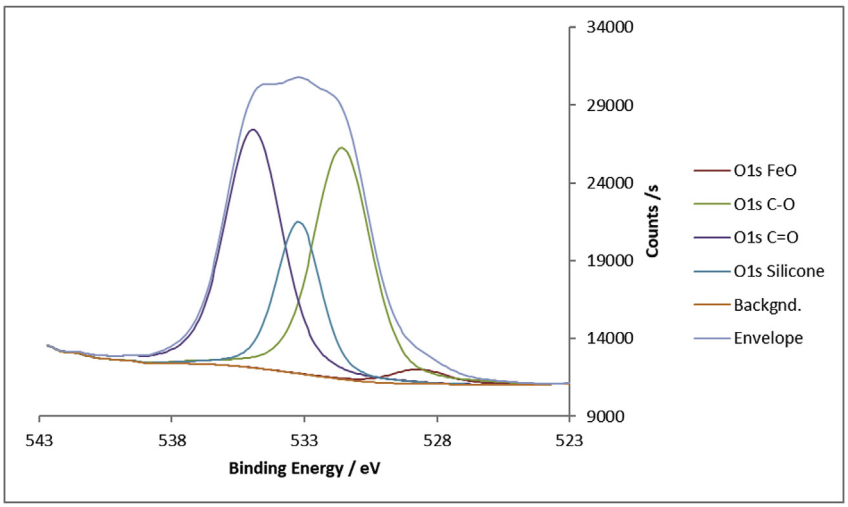

Fig. 9. High resolution O1s scan at TDC.

numerical model. The roughness parameter and typical asperity slope were determined to be 0.110 and 0.0161 respectively.

A graph showing the agreement (less than 5% difference) between the surface $F_{5/2}(\lambda)$ and that calculated for a Gaussian peak height is presented in Fig. 4.

An example of the surface roughness data collected from the liner can be seen in Fig. 5. The data is obtained using an Alicona G4 microscope, implementing the focus variation technique.

Viscous friction f_v, is found as:

$$f_v = \int\int \tau dxdy \tag{5}$$

$$\tau = -\frac{dp}{dx}\frac{h}{2} + \frac{\eta U}{h} \tag{6}$$

The lubricant pressure distribution p is calculated from the Reynolds equation solution together with geometrical and rheological state equations through a finite difference solution method.

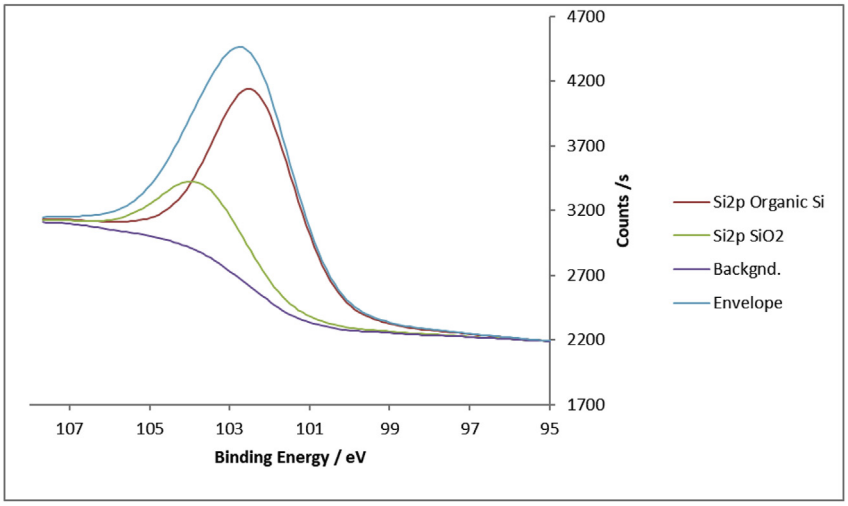

Fig. 10. High resolution Si2p scan at TDC.

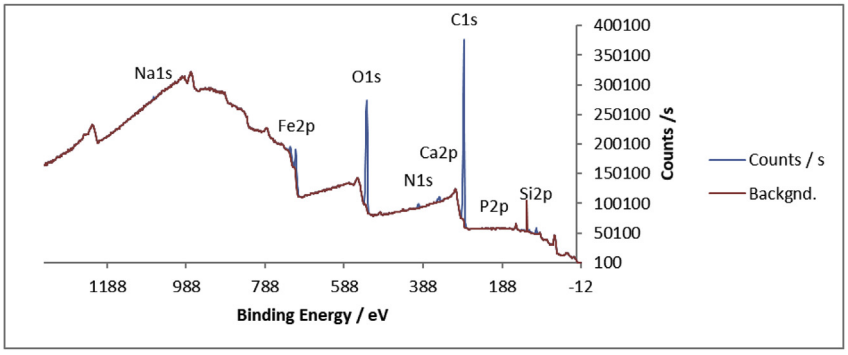

Fig. 11. XPS spectra analysis of mid-stroke.

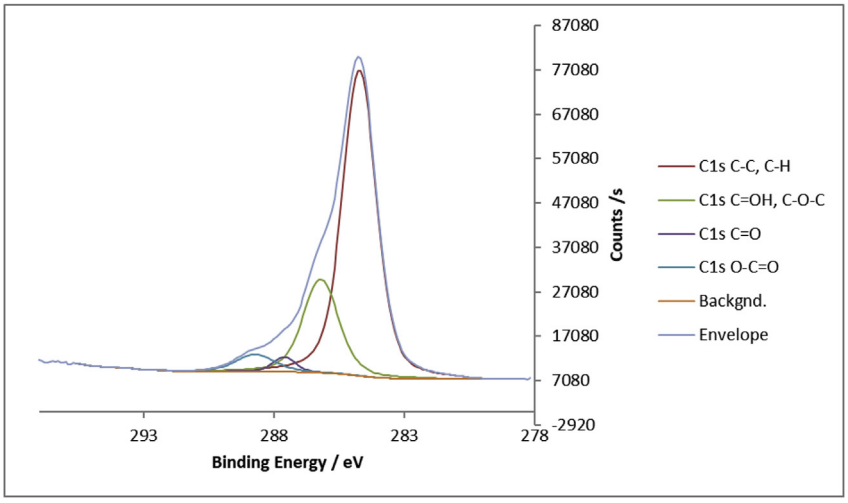

Fig. 12. High resolution C1s scan at mid-stroke.

4.2. Numerical solution of Reynolds equation

The oil pressure distribution is required. The 2D Reynolds equation for a compressible piezo-viscous lubricant is:

$$\frac{\partial}{\partial x}\left(\frac{\rho h^3}{6\eta}\frac{\partial p}{\partial x}\right)+\frac{\partial}{\partial y}\left(\frac{\rho h^3}{6\eta}\frac{\partial p}{\partial y}\right)=\frac{\partial(\rho U h)}{\partial x}+\frac{\partial(\rho V h)}{\partial y}+2\frac{\partial(\rho h)}{\partial t} \quad (7)$$

The lubricant flow in the direction of entraining motion *x (this is the axial direction of the ring)* is included in the above formulation. Side-leakage *y (this is the circumferential direction of the ring)* is also included, however, for the purpose of this study the Couette flow is neglected as it is assumed that the velocity in the circumferential direction is equal to zero, $V = 0$, and thus no side leakage. In the analysis the lubricant is considered to be Newtonian due to low shear.

The change in lubricant density in respect to pressure as well as temperature is given as [22]:

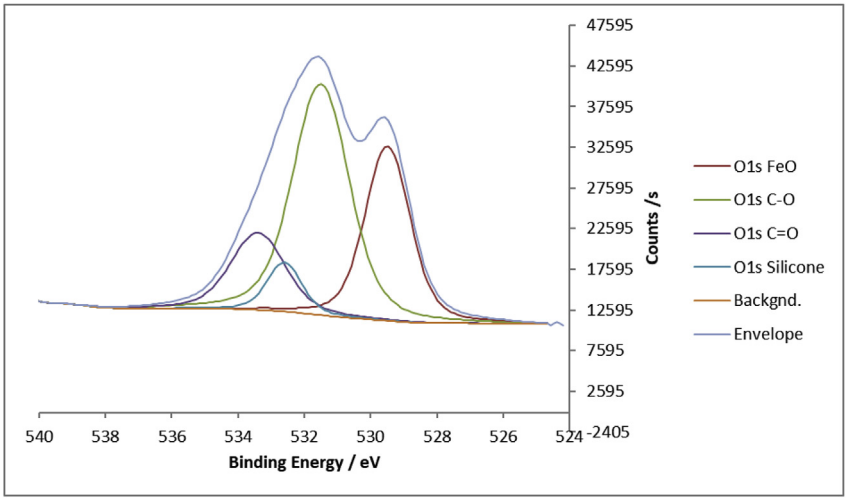

Fig. 13. High resolution O1s scan at mid-stroke.

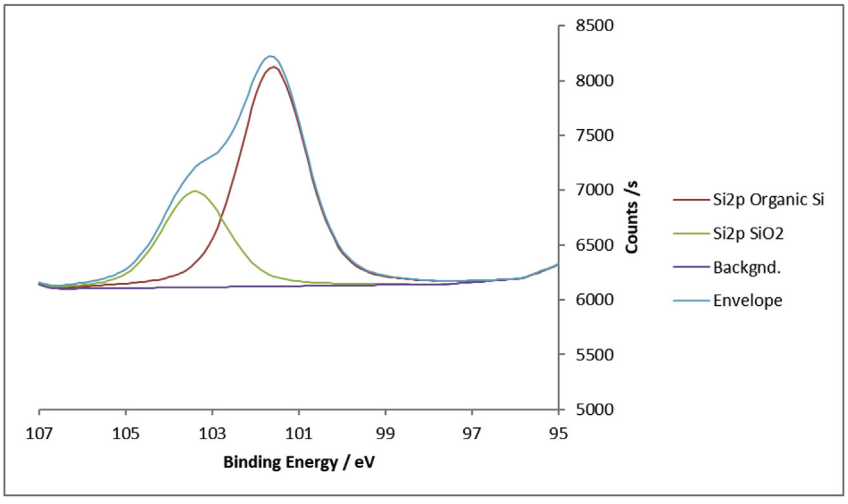

Fig. 14. High resolution Si2p scan at mid-stroke.

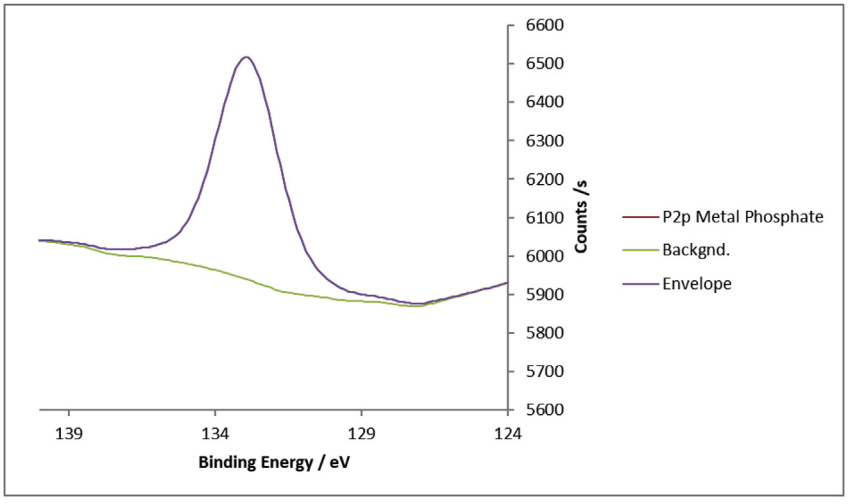

Fig. 15. High resolution P2p scan at mid-stroke.

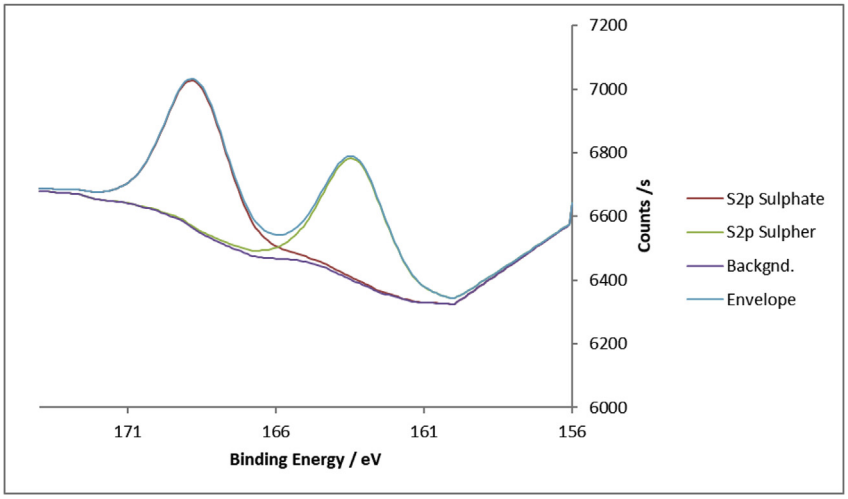

Fig. 16. *High resolution S2p scan at mid-stroke.*

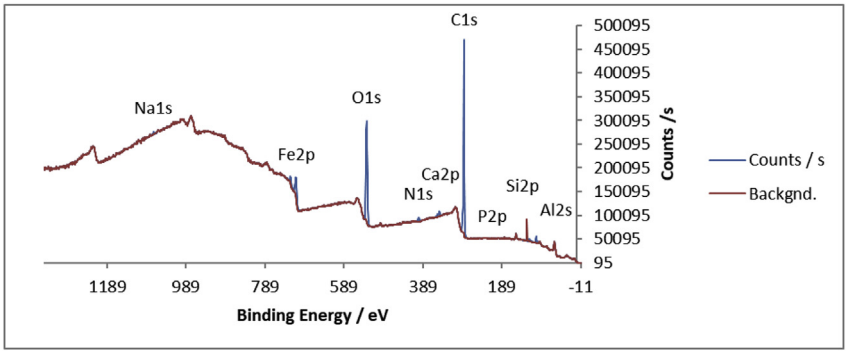

Fig. 17. XPS spectra analysis of BDC.

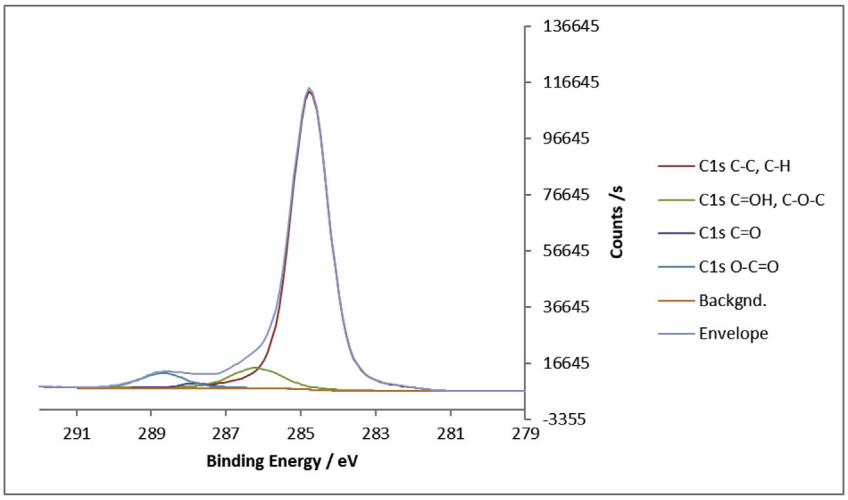

Fig. 18. High resolution C1s scan at BDC.

$$\rho = \rho_0\left(1 + \frac{0.6 \times 10^{-9}(p - p_0)}{1 + 1.7 \times 10^{-9}(p - p_0)}\right)[1 - 0.65 \times 10^{-3}(\theta - \theta_0)] \tag{8}$$

where at ambient pressure ρ_0 is the lubricant density with a reference temperature θ_0 and p is the absolute pressure. Barus law is widely utilised to find the viscosity of a lubricant [23]. This approach was extended by Roelands [24] and Houpert [25]:

$$\eta = \eta_0(\alpha^* p) \tag{9}$$

$$\alpha^* p = [\ln(\eta_0 + 9.67)]\left\{\left(\frac{\theta - 138}{\theta_0 - 138}\right)^{-S_0}\left[\left(1 + \frac{p}{p_0}\right)^Z - 1\right]\right\} \tag{10}$$

where Z and S_0 are:

$$Z = \frac{\alpha}{5.1 \times 10^9[\ln(\eta_0) + 9.67]} \tag{11}$$

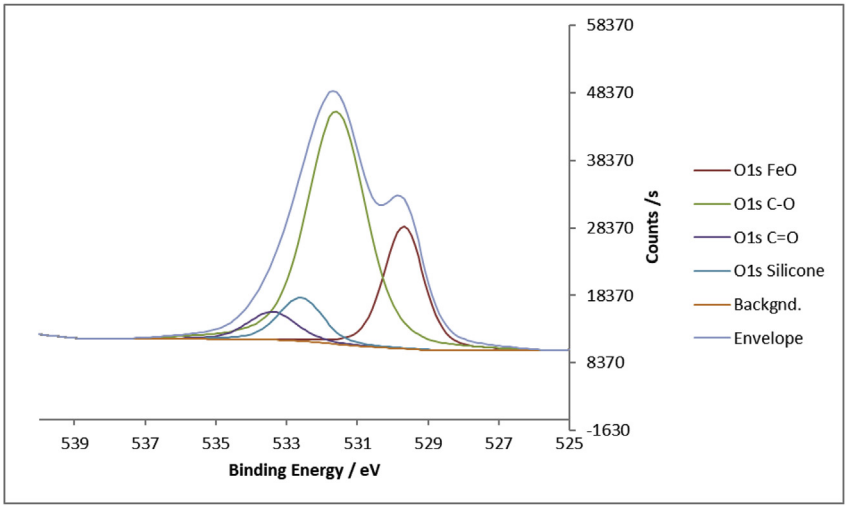

Fig. 19. High resolution O1s scan at BDC.

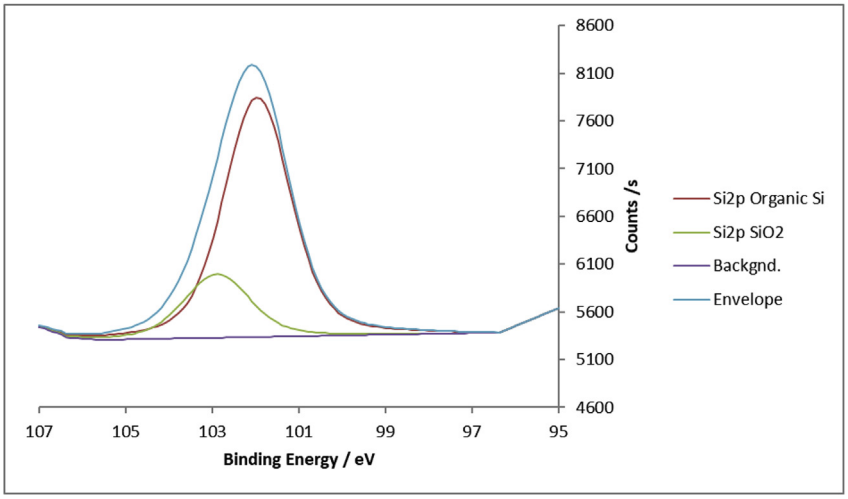

Fig. 20. High resolution Si2p scan at BDC.

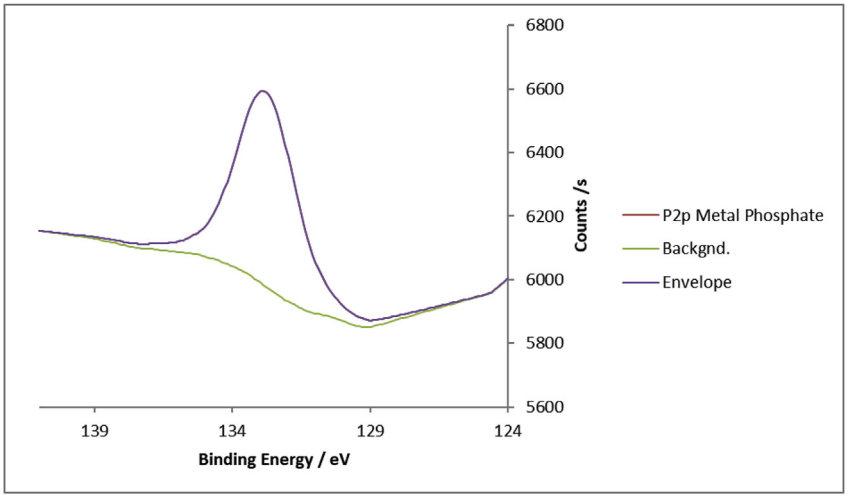

Fig. 21. High resolution P2p scan at BDC.

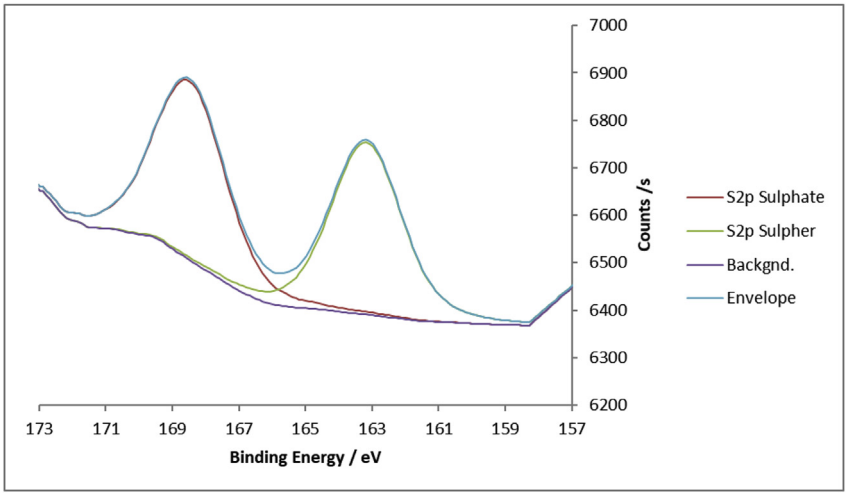

Fig. 22. High resolution S2p scan at BDC.

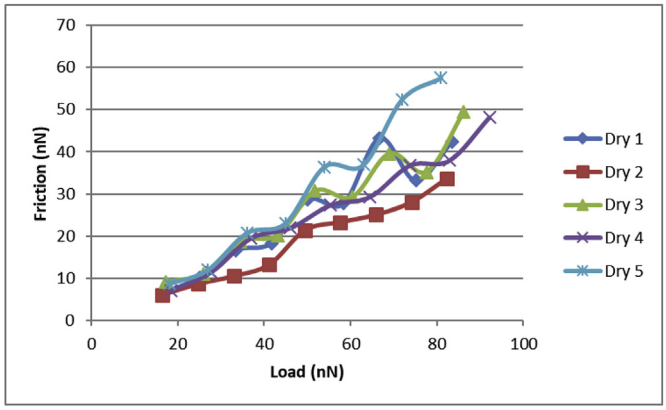

Fig. 23. Measured LFM results for dry contact at TDC.

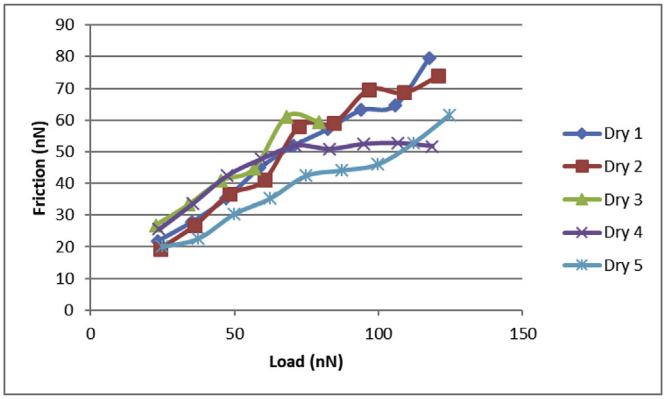

Fig. 25. Measured LFM results for dry contact at mid-stroke.

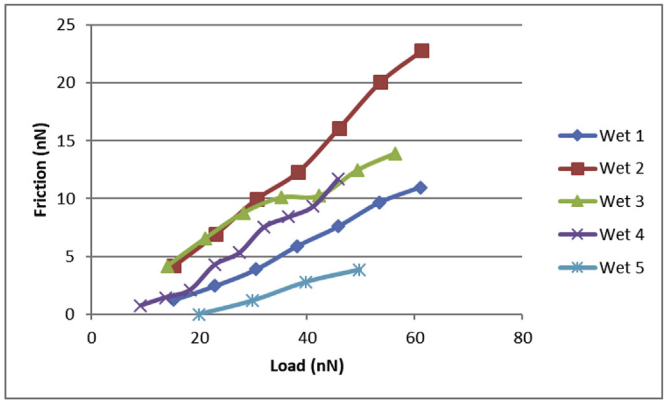

Fig. 24. Measured LFM results for wet contact at TDC.

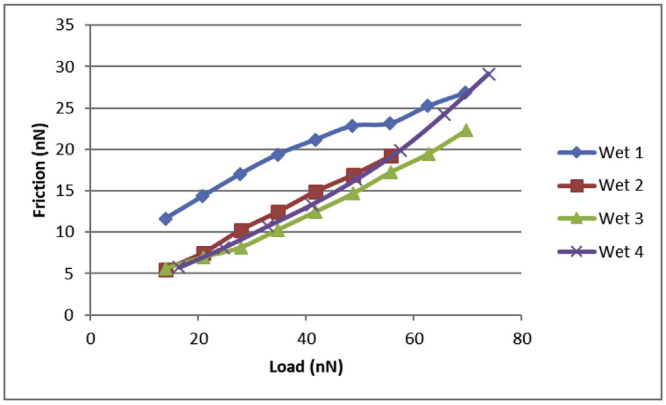

Fig. 26. Measured LFM results for wet contact at mid-stroke.

$$S_0 = \frac{\beta(\theta_0 - 138)}{\ln(\eta_0) + 9.67} \tag{12}$$

The minimum film thickness is h_m. The film thickness distribution is then obtained as:

$$h(x, t) = h_m(t) + h_s(x) \tag{13}$$

Bolander et al. [26] and Mishra et al. [27] show that the deflection within the contact can be considered negligible due to insufficient contact pressure which is generated. Baker et al. [28] have shown the modal response of the rings, however, for the purpose of this study, the dynamic behaviour is not considered.

4.3. Assuming a parabolic ring profile

$$h_s(x) = \frac{c\left(x - {}^{b}/_{2}\right)^2}{\left({}^{b}/_{2}\right)^2} \tag{14}$$

The generated pressure in the conjunction should be able to oppose the externally applied force (Fig. 6). The forces acting on the cylinder as a result of the ring pushing outwards are:

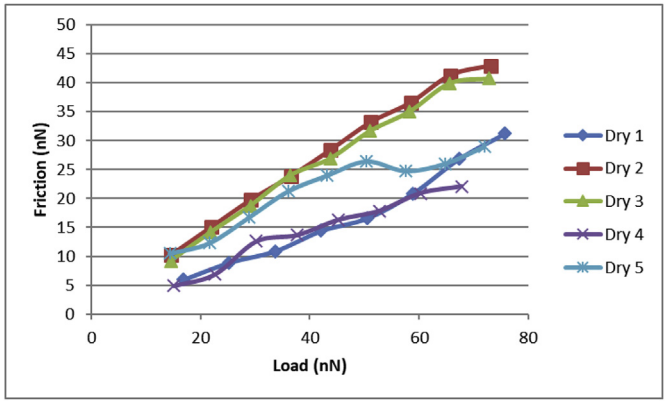

Fig. 27. Measured LFM results for dry contact at BDC.

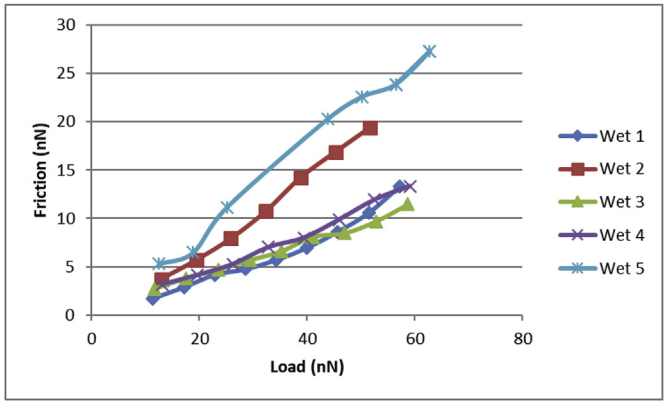

Fig. 28. Measured LFM results for wet contact at BDC.

Table 5
Average measured LFM results.

Zone	TDC	Mid-Stroke	BDC
ς (dry)	0.591	0.594	0.487
Variance (dry)	0.047	0.013	0.012
Standard Deviation (dry)	0.216	0.116	0.109
ς (wet)	0.253	0.347	0.308
Variance (dry)	0.011	0.003	0.012
Standard Deviation (dry)	0.104	0.062	0.135
Rq	0.284	0.329	0.295
Sq	0.359	0.388	0.397

Table 6
Engine data.

Parameters	Values	Units
Torque	52.03	Nm
No. of cylinders	4	–
Engine type	Diesel	–
Crank-pin radius, r	39.75	mm
Connecting rod length, l	138.1	mm
Bore nominal radius, r_0	44.52	mm
Ring crown height, c	10	μm
Ring axial face-width, b	1.15	mm
Ring radial width, d	3.5	mm
Ring free end-gap, g	10.5	mm

$$F = F_e + F_g \tag{15}$$

F_g acts radially as a result of the combustion pressure, p_g: Fig. 30.

$$F_g = p_g bl \tag{16}$$

Table 7
Material properties of the piston ring.

Parameters	Values	Units
Ring material	Steel SAE 9254	–
Modulus of elasticity of the ring	203	GPa
Poisson's ratio of the ring	0.30	–
Density of the ring material	7700	kg/m^3

The ring tension, F_e, assuming a rectangular cross section can be found using the elastic pressure acting on the ring, p_e:

$$F_e = p_e bl \tag{17}$$

$$p_e = \frac{gEI}{3\pi b r_0^4} \tag{18}$$

$$I = \frac{1}{12} bd^3 \tag{19}$$

Many hydrodynamic and mixed lubrication models for the piston ring - cylinder liner conjunction assume the inlet to be fully flooded [29–32], thus assuming there is sufficient lubricant available for the rings at all angles of the crank cycle. For this analysis, this assumption is also used and the position of the inlet is assumed to be the edge of the ring thus:

$$p_{x=-b/2} = P_a \tag{20}$$

The outlet boundary condition used in this analysis is Reynolds (or Swift-Steiber [33,34]). This has been proven to be an accurate method for applying the outlet boundary as was shown by Arcoumanis et al. [35], who experimentally observed that their predictions made using the Swift-Steiber boundary conditions were in good agreement with the measurements recorded. The exit boundary conditions is:

$$\begin{cases} p_{x=x_c} = P_{cav} \\ \frac{\partial p}{\partial x}\Big|_{x=x_c} = 0 \end{cases} \tag{21}$$

This analysis assumes that $P_{cav} = P_{atmospheric}$, at $x = x_c$.

5. Results and discussion

The AFM measurement is carried out in order to investigate the effect of considering the real surface on the boundary friction. The XPS measurement is conducted to understand the composition of liner surface comprising formation of a tribo-film as well as adsorbed deposits. Finally, these values have been used for predictions with the numerical solutions in section 4 in order to observe the effect of measured values on the total conjunctional friction.

5.1. XPS of Top Dead Centre

Fig. 7 shows the chemical spectrum at TDC with several deposits, largely of Carbon, Oxygen and Silicon having large dominant peaks. Approximately 60 wt% of the particles are Carbon based and 30 wt% are Oxygen products. This is in line with the findings of Buhaug [6], where the composition of piston varnish was traced.

High resolution analysis shows that many different forms of carbon are formed within the TDC region (Fig. 8). Carbon black and carbon monoxide deposits are both present as the result of incomplete combustion. The oxygen scan (Fig. 9) supports what is seen in the carbon data, with the addition of both iron and silicon. Silicon-based oil has been used in the automotive as an additive for many conjunctions where cooling issues are of paramount importance. The organic silicon present in Fig. 10 is due to the use of silicon-based oil and was present in all regions of the liner studied.

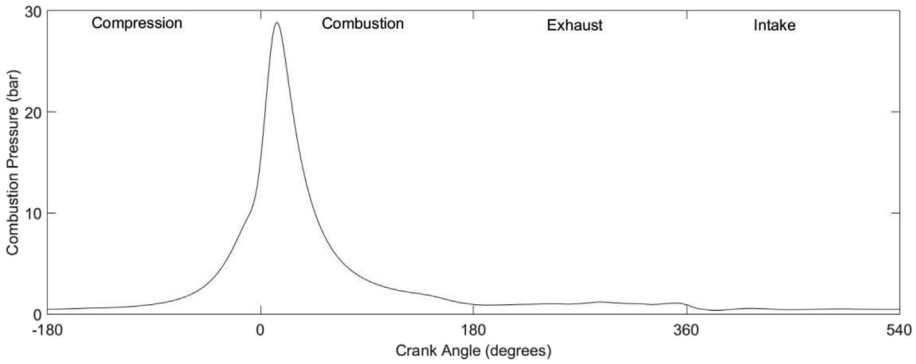

Fig. 29. Combustion chamber pressure.

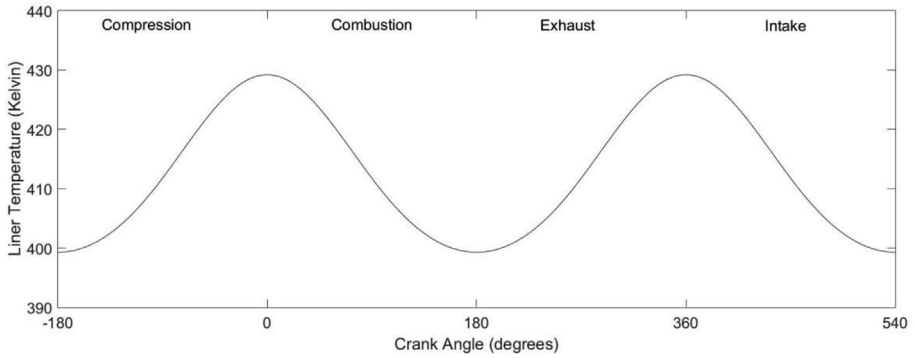

Fig. 30. Liner temperature.

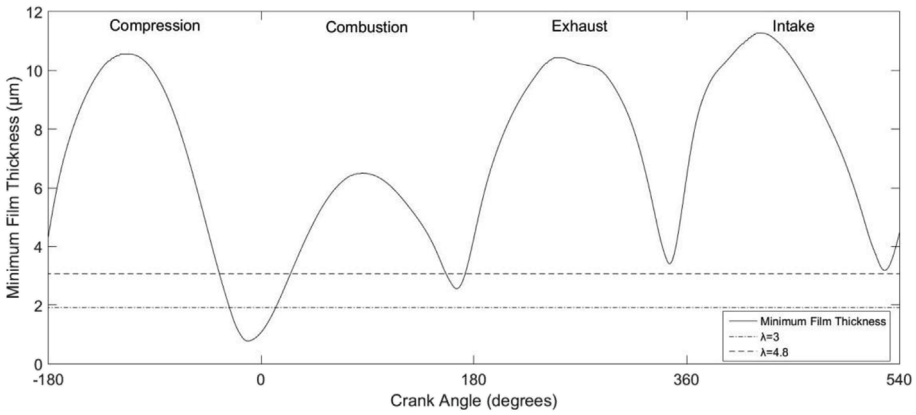

Fig. 31. Minimum film thickness of the top compression ring.

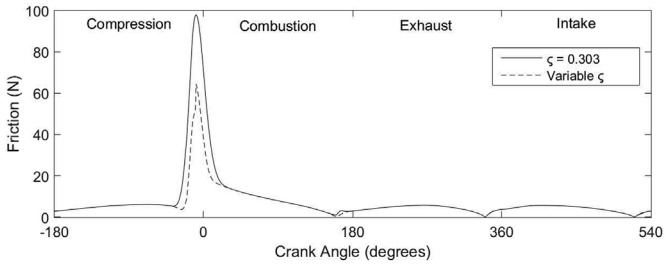

Fig. 32. Total friction for the top compression ring.

5.2. XPS mid-stroke

Analysis of the elemental spectrum for the mid-stoke liner region is similar to that at TDC where carbon, oxygen and silicon are present on the surface of the liner (Figs. 11–14). It is interesting to note the presence of sulphur and phosphorous also at the mid-stroke position (Figs. 15 and 16). Phosphorous is a constituent of ZDDP, an anti-wear agent often used in additive packages, and sometimes paired with sulphur for anti-oxidation. The sulphur is also likely to be a deposit of diesel fuel used in combustion during the engine testing as well as often present in the substrate material.

5.3. XPS bottom dead centre

A similar level of deposition can also be seen at BDC. Again, the typical components of varnish are dominant in the spectra analysis, detected alongside silicon, phosphates and sulphur. These can be seen in Figs. 17–22.

5.4. Measurement of boundary shear strength ς

Measurements have been taken for the three regions identified on

the liner, TDC, Mid-Stroke and BDC, for both dry and wet contact friction using LFM. The value of ς is represented by the gradient of each line in Figs. 23–28 with dry or wet LFM.

Table 5 Presents the averaged results of the measured LFM data for all regions under both dry and wet contact conditions. The measured results are taken across a scanned area of $4 \times 1\,\mu m^2$, with 1024×256 data points for each area. As is revealed from results, each zone has its own coefficient of boundary shear strength and thus its own frictional characteristics. This is because of the prevailing contact conditions; comprising varying regime of lubrication, generated pressures, shear and temperature. These yield different levels of energy which affect the activation of various lubricant additives, bonding or adsorbing them onto the liner surface. These varied cyclic conditions also affect the localised adsorption of combustion by-products. Therefore, it should be noted that the use of a single average value to calculate boundary friction in any analysis of boundary friction would not be truly representative of the interacting surfaces. In fact, under wet conditions in particular the ς value varies considerably. This is likely due to the large amount of deposits which have been found using XPS analysis.

It can be seen in Figs. 23–28 that there is range of results, hence the quantity of repetitions which were made for this analysis to obtain the most representative result set possible. This effect could be because of tribofilm or substrate interactions on the sample liner as the term ς accounts for the resistancet to shear at the contact of two asperities (a surface effect). Thus, if the surface material combination is a tribofilm the ς represents a tribolfilm and likewise if the combination is substrate to substrate, $\varsigma\varsigma$ will be for the substrate.

5.5. Simulation of top ring-cylinder liner conjunction

A C-segment vehicle with a four cylinder, four stroke diesel engine is used in the current study. Surface parameters and material properties are listed in Table 1, oil rheological data in Table 2 and Engine data in Table 6. Material properties of the ring used in the analysis are presented in Table 7. This study uses a passenger car engine at the running speed of 1500 rpm, analogous to 35 km/h on the New European Driving Cycle (NEDC) whilst the vehicle is in 3rd gear. The output torque is 52.03 Nm. For the described conditions, a numerically generated combustion pressure is presented in Fig. 29 and the corresponding liner temperature in Fig. 30.

Fig. 31 shows the predicted minimum film thickness for every crank angle, as well as the plot of $\lambda = 4.8$ and $\lambda = 3$, below which the film thickness falls into the mixed and boundary regime of lubrication. This is of particular importance during the compression and combustion strokes, as it signifies that boundary interactions will dominate over viscous friction. This is shown in Fig. 32, where the effect of a variable ς is seen to reduce the maximum friction by almost 30%. This is comparable to the experimental findings of Gore et al. [36], where it was found that boundary interactions are dominant in the combustion stroke.

6. Concluding remarks

Previous simulations have used single averaged values for the key parameter: ς, obtained from idealistic flat surfaces, sometimes in combination with a partially formulated lubricant or under dry surface condition. This study shows that this assumption can lead to inaccurate prediction of boundary friction, particularly during the combustion stroke, where boundary friction is dominant.

The paper presents measurements of ς from a used real cylinder liner surface which takes into account the effect of presence of depositions and tribo-films on the liner surface in combination with a fully formulated lubricant. It has been found that the value of ς varies in three different distinct regions of a used cylinder liner.

The acquired XPS spectra are used to identify chemical composition of liner surface regions, including all depositions and tribo-film constituents, not previously reported for actual liners of vehicles in open literature. Depositions on the surface because of combustion during running of the engine, in particular piston varnish, are found on the liner at locations corresponding to high ς values.

The combined precision measurements and numerical analysis presented in this paper show the importance of using measured data for simulations. It was found that the total friction for a top compression ring can vary as much as 30% between the compression and combustion stroke by using a variable value of ς.

It is found that there is a requirement for further analysis on used engine components run under normal operating conditions, rather than unrepresentative smooth flat surfaces for measurement of surface conditions.

Acknowledgement

The authors of this work wish to show their thanks to the Engineering and Physical Sciences Research Council (EPSRC) and to our industrial collaborators AVL List GmbH for the financial and technical contributions they have made to this research.

References

[1] Holmberg K, Andersson P, Nylund N-O, Mäkelä K, Erdemir A. Global energy consumption due to friction in trucks and buses. Tribol Int 2012;47:221–34.
[2] Holmberg K, Andersson P, Erdemir A. Global energy consumption due to friction in passenger cars. Tribol Int 2012;47:221–34.
[3] Kittelson, D.B., Ambs, J.L., and Hadjkacem, H., "Particulate emissions from diesel engines: influence of in-cylinder surface", SAE 900645, International Congress and Exposition, Detroit Michigan, February 26 – March 2, 1990.
[4] Weiss EK, Busenthuer BB, Hardenberg HO. Diesel fuel sulfur and cylinder liner wear of heavy-duty diesel engine. SAE, Pap. 1987;872148.
[5] Naylor MG, Kodali P, Wang JC. Diesel engine tribology. In: Bhushan B, editor. Modern tribology handbook volume 2 materials, coatings, and industrial applications. CRC Press LLC; 2001.
[6] Buhaug O. Deposit formation on cylinder liner surfaces in medium-speed engines Doctoral Thesis submitted at the Norwegian University of Science and Technology 2003
[7] Taylor RI, Coy RC. Improved fuel efficiency by lubricant design: a review. Proc. IMechE, Part J: J. Engineering Tribology 2000;214(1):1–15.
[8] Gore M, Rahmani R, Rahnejat H, King PD. Assessment of friction from compression ring conjunction of a high-performance internal combustion engine: a combined numerical and experimental study. Proc. IMechE, Part C: J Mech Eng Sci 2016;230(12):2073–85.
[9] Greenwood JA, Tripp JH. The contact of two nominally flat rough surfaces. Proc. IMechE 1970-1971;185:625–34.
[10] Greenwood JA, Tripp JH. The elastic contact of rough spheres. J Appl Mech 1967;34(1):153–9.
[11] Meyer G, Amer NM. Simultaneous measurement of lateral and normal forces with an optical beam deflection atomic force microscope. Appl Phys Lett 1990;57:2089–91.
[12] Bhushan B, Marti O. Scanning probe microscopy–principle of operation, instrumentation, and probes. Springer handbook of nanotechnology. Springer Berlin Heidelberg; 2004. p. 325–69.
[13] Styles G, Rahmani R, Rahnejat H, Fitzsimons B. "In-cycle and life-time friction transience in piston ring–liner conjunction under mixed regime of lubrication". Int J Engine Res 2014;15(7):862–76.
[14] Chong WWF, Rahnejat H. Nanoscale friction as a function of activation energies. Surf Topogr Metrol Prop 2015;3(4):044002.
[15] Ahimou F, Semens MJ, Novak PJ, Haugstad G. Biofilm cohesiveness measurements using a novel atomic force microscopy methodology. Appl Environ Microbiol 2007;73(9):2897–904.
[16] Buenviaje CK, Ge SR, Rafailovich MH, Overney RM. Atomic force microscopy calibration methods for lateral force, elasticity, and viscosity. MRS proceedings, vol. 522. Cambridge University Press; 1998. p. 187.
[17] Van der Heide P. X-ray photoelectron spectroscopy: an introduction to principles and practices. John Wiley & Sons; 2011.
[18] Gohar R, Rahnejat H. Fundamentals of tribology. London: Imperial College Press; 2008.
[19] Teodorescu M, Kushawa M, Rahnejat H, Rothberg SJ. Multi-physics analysis of valve train systems: from system level to microscale interactions. Proc. IMechE PartK: J. Multi-body Dynamics 2007;221(3):349–61.
[20] Leighton M, Nicholls T, De la Cruz M, Rahmani R, Rahnejat H. Combined lubricant–surface system perspective: multi-scale numerical–experimental investigation. Proc. IMechE, Part J: J. Engineering Tribology 2017;231(7):910–24.
[21] Eyring H. Viscosity, plasticity, and diffusion as examples of absolute reaction rates. J. chemical physics 1936;4(4):283–91.
[22] Dowson D, Higginson GR. Elasto-hydodynamic lubrication. 2nd SI edition Oxford: Pergamon Press; 1977.

[23] Barus C. Isothermals isopietics and isometrics in relationship to viscosity. American J. Science, 3rd Series 1893;45:87–96.
[24] Roelands CJ. Correlation aspects of the viscosity-temperature-pressure relationships of lubricating oils PhD thesis the Netherlands: Delft University of Technology; 1966
[25] Houpert L. New results of traction force calculations in elastohydrodynamic contacts. Trans. ASME, J. Tribology 1985;107:241–8.
[26] Bolander NW, Steenwyk BD, Sadeghi F, Gerber GR. Lubrication regime transitions at the piston ring-cylinder liner interface. Proc. IMechE, Part J: J. Engineering Tribology 2005;219(1):19–31.
[27] Mishra PC, Balakrishnan S, Rahnejat H. Tribology of compression ring-to-cylinder contact at reversal. Proc. IMechE, Part J: J. Engineering Tribology 2008;222(7):815–26.
[28] Baker C, Theodossiades S, Rahmani R, Rahnejat H, Fitzsimons B. On the transient three-dimensional tribodynamics of internal combustion engine top compression ring. J Eng Gas Turbines Power 2017;139(6):062801.
[29] Morris N, Rahmani R, Rahnejat H, King PD, Fitzsimons B. Tribology of piston compression ring conjunction under transient thermal mixed regime of lubrication. Tribol Int 2012;59:248–58.
[30] Rahmani R, Theodossiades S, Rahnejat H, Fitzsimons B. Transient elastohydrodynamic lubrication of rough new or worn piston conjunction with an out-of-round cylinder bore. Proc. IMechE, Part J: J Engineering Tribology 2012;226(4):284–305.
[31] Bewsher SR, Turnbull R, Mohammadpour M, Rahmani R, Rahnejat H, Offner G, Knaus O. Effect of cylinder de-activation on the tribological performance of compression ring conjunction. Proc. IMechE, Part J: J. Engineering Tribology 2016;231(8):997–1006.
[32] Akalin O, Newaz GM. Piston ring-cylinder bore friction modelling in mixed lubrication regime: part I – analytical results. Trans. ASME, J. Tribology 1999;123(1):211–8.
[33] Swift HW. The stability of lubricating films in journal bearings. Proc Inst Civ Eng 1932;233:267–88.
[34] Steiber W. Das-Schwimmlager: hydrodynamische Theorie des Gleitlagers no. V.D.I., Berlin 1933. p. 106.
[35] Arcoumanis C, Duszynski M, Flora H, Ostovar P. Development of a piston-ring lubrication test-rig and investigation of boundary conditions for modelling lubricant film properties SAE Technical Paper 952468 1995.
[36] Gore M, Theaker M, Howell-Smith S, Rahnejat H, King P. Direct measurement of piston friction of internal-combustion engines using the floating-liner principle. Proc. IMechE, Part D: J. Automobile Engineering 2014;228(3):334–54.